JACS
JOURNAL OF THE AMERICAN CHEMICAL SOCIETY
Article
pubs.acs.org/JACS

Thermoelectrics with Earth Abundant Elements: High Performance p-type PbS Nanostructured with SrS and CaS

Li-Dong Zhao,[†,#] Jiaqing He,[†,‡,#] Chun-I Wu,[§] Timothy P. Hogan,[§] Xiaoyuan Zhou,[∥] Ctirad Uher,[∥] Vinayak P. Dravid,[‡] and Mercouri G. Kanatzidis*[,†,⊥]

[†]Department of Chemistry, and [‡]Department of Materials Science and Engineering, Northwestern University, Evanston, Illinois 60208, United States

[§]Department of Electrical and Computer Engineering, Michigan State University, East Lansing, Michigan 48824, United States

[∥]Department of Physics, University of Michigan, Ann Arbor, Michigan 48109, United States

[⊥]Materials Science Division, Argonne National Laboratory, Argonne, Illinois 60439, United States

Supporting Information

ABSTRACT: We report high thermoelectric performance in nanostructured p-type PbS, a material consisting of highly earth abundant and inexpensive elements. The high level of Na doping switched intrinsic n-type PbS to p-type and substantially raised the power factor maximum for pure PbS to ~9.0 μW cm^{-1} K^{-2} at >723 K using 2.5 at. % Na as the hole dopant. Contrary to that of PbTe, no enhancement in the Hall coefficient occurs at high temperature for heavily doped p-type PbS, indicating a single band model and no heavy hole band. We also report that the lattice thermal conductivity of PbS can be greatly reduced by adding SrS or CaS, which form a combination of a nanostructured/solid solution material as determined by transmission electron microscopy. We find that both nanoscale precipitates and point defects play an important role in reducing the lattice thermal conductivity, but the contribution from nanoscale precipitates of SrS is greater than that of CaS, whereas the contribution from point defects in the case of CaS is greater than that of SrS. Theoretical calculations of the lattice thermal conductivity based on the modified Callaway model reveal that both nanostructures and point defects (solid solution) effectively scatter phonons in this system. The lattice thermal conductivity at 723 K can be reduced by ~50% by introducing up to 4.0 at. % of either SrS or CaS. As a consequence, *ZT* values as high as 1.22 and 1.12 at 923 K can be achieved for nominal $Pb_{0.975}Na_{0.025}S$ with 3.0 at. % SrS and CaS, respectively. No deterioration was observed after a 15 d annealing treatment of the samples, indicating the excellent thermal stability for these high performance thermoelectrics. The promising thermoelectric properties of nanostructured PbS point to a robust low cost alternative to other high performance thermoelectric materials.

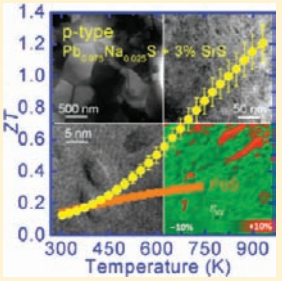

INTRODUCTION

Thermoelectric materials capable of creating electricity from waste heat sources can play an important role in energy conservation and production.[1,2] The efficiency of thermoelectric materials is determined by the dimensionless figure of merit (*ZT*), defined as $ZT = (S^2\sigma/\kappa)T$, where *S*, σ, κ, and *T* are the Seebeck coefficient, electrical conductivity, thermal conductivity, and absolute temperature, respectively. In addition to high *ZT*, both n- and p-type materials with similar thermoelectric performance and compatible mechanical properties are needed to construct an efficient thermoelectric device.

Thermoelectric materials are classified on the basis of their applicable temperature range. For near-room-temperature applications up to 500 K, Bi_2Te_3 alloys currently possess the highest *ZT* for both n-type[3] and p-type[4] systems. For mid-temperature (500−900 K) thermoelectric materials, PbTe-based alloys are widely used. High-temperature (>900 K) thermoelectric generators have typically used SiGe alloys for both n-type[5] and p-type[6] legs. The biggest advances in this field have been achieved in nanostructured PbTe-based materials in which very low thermal conductivity can be obtained, resulting in the highest *ZT* values among all thermoelectrics. To date, both n-type (e.g., $AgPb_mSbTe_{m+2}$,[7,8] $Pb_{1-x}Sn_xTe$−PbS,[9] PbTe−CdTe,[10] and PbTe−Ag_2Te[11]) and p-type (e.g., $AgPb_mSn_nSbTe_{m+n+2}$,[12] $PbTe_{1-x}Se_x$,[13] $NaPb_mSbTe_{m+2}$,[14] PbTe−SrTe,[15] and PbTe−PbS[16]) materials have been developed. These materials, however, all contain a significant amount of Te, which is scarce in the earth's crust. To allow for widespread use of thermoelectrics in a variety of applications, inexpensive alternatives are needed. In this context, attention is now turning to materials such as PbSe and PbS.[17−19]

PbS is an ideal candidate because S is more abundant and less expensive than both Se and Te. Recently, we investigated the thermoelectric properties of compositions lying on the PbS-rich side of the PbS−PbTe phase diagram and reported that significant thermoelectric enhancements for n-type samples can be achieved.[20] This motivated us to expand our investigations to Te-free PbS-based systems and utilize many of the new concepts and ideas developed for PbTe, which have been so

Received: February 22, 2012
Published: April 13, 2012

   dx.doi.org/10.1021/ja301772w | J. Am. Chem. Soc. 2012, 134, 7902−7912

Table 1. Some Physical Properties for Pb-Based Chalcogenides and the Maximum *ZT* Values Reported So Far

PbQ, Q = Te, Se, S	melting point (K)	band gap (eV)	earth abundance Q,[a] (ppm)	*ZT*, n-type	*ZT*, p-type
PbTe	∼1197	0.31	∼0.001	$AgPb_{18}SbTe_{20}$,[b] 1.8 at 800 K	PbTe+12%PbS+2%Na,[c] 1.8 at 800 K
PbSe	∼1352	0.28	∼0.05	PbSe+12%PbS+0.3%$PbCl_2$,[d] 1.3 at 900 K	$Pb_{0.993}Na_{0.007}Se$,[e] 1.2 at 850 K
PbS	∼1391	0.41	∼420	PbS+1%Bi_2S_3+1%$PbCl_2$,[f] 1.1 at 923 K	PbS+3%SrS+2.5%Na,[g] 1.2 at 923 K

[a]Reference 25. [b]Reference 7. [c]Reference 16. [d]Reference 17. [e]Reference 19. [f]Reference 21. [g]This work.

successful in producing its record-breaking performance.[9−16] Indeed, for n-type PbS we showed dramatic improvements in *ZT* from 0.4 to 1.1 at 923 K by combining nanoprecipitates of Bi_2S_3 and Sb_2S_3 second phases with heavy $PbCl_2$ doping.[21] A comparison of some physical properties for optimized, high-performance n- and p-type Pb-based chalcogenide thermoelectric materials is listed in Table 1.

In this Article, we show that vast improvements in *ZT* can also be achieved in p-type PbS materials. We chose Na as the p-type dopant to tune the carrier concentration by substituting Na^+ for Pb^{2+} to optimize the electrical transport properties for the PbS matrix. We find that, unlike in the n-type samples, precipitates of Bi_2S_3 and Sb_2S_3 are not suitable for creating p-type PbS samples. Instead, SrS and CaS were found to be excellent second phases to create nanostructures and dramatically reduce the lattice thermal conductivity. We then applied the spark plasma sintering (SPS) technique to densify the samples. SPS is a suitable and effective technique to rapidly fabricate relatively high density, robust, and fine-grained thermoelectric materials.[22] Our results show that these nanoscale phases of SrS and CaS greatly reduce the lattice thermal conductivity of p-type PbS to levels similar to those achieved in nanostructured PbTe.[7,9−16] As a result, we have obtained a *ZT* value of 1.20 at 923 K for p-type PbS nanostructured with 3.0 at. % SrS and doped with 2.5 at. % Na. This is even higher than that reported for the n-type PbS-based system.[20,21] In addition, these high thermoelectric performance lead sulfide compounds appear to have excellent thermal stability, as indicated by the stability of the properties after a 15 d annealing treatment. PbS contains the least expensive elements among any high *ZT* thermoelectric materials under consideration today, including Zn_4Sb_3 and $Mg_2Si_{1-x}Sn_x$.[23] The results reported here for nanostructured p-type PbS are significant because, along with those reported previously for the n-type system,[20,21] PbS is now a complete and low-cost system that rivals the best thermoelectric materials in existence including other heavier lead chalcogenides,[17−19] zinc antimony,[1] magnesium silicide,[23] skutterudites,[24] and silicon−germanium alloys.[5,6]

EXPERIMENTAL SECTION

Synthesis. Reagent chemicals were used as obtained: Pb wire (99.99%, American Elements, U.S.), S shot or chunk (99.999%, Inc., Canada), Sr chunk (99.9%, Cerac, U.S.), Ca redistilled granule (99.5%, Alfa Aesar, U.S.), and Na chunk (99.999%, Aldrich, U.S.).

Synthesis of Starting Materials. PbS containing SrS or CaS and doped with Na was prepared as follows: $Pb_{1-x}Na_xS$ (x = 0, 0.01, 0.02, 0.025, 0.03, and 0.04) samples were synthesized by a melting reaction using elemental Pb, S, and Na inside carbon-coated fused quartz tubes. The tubes were then evacuated to a pressure of ∼10^{-4} Torr, flame-sealed, slowly heated to 723 K in 12 h, then to 1423 K in 7 h, soaked at this temperature for 6 h, and subsequently water quenched to room temperature. SrS/CaS was synthesized using elemental Sr/Ca and S inside an Al_2O_3 crucible that was placed in a quartz tube. The quartz tubes were evacuated to a pressure of ∼10^{-4} Torr, sealed, slowly heated to 1153 K in 30 h, soaked at this temperature for 10 h, and subsequently cooled to room temperature in 12 h.

Na-doped PbS ingots were crushed carefully into powders in air and melted with y% (mol fraction in the text) of the second phases SrS/CaS (y = 0, 1.0, 2.0, 3.0, and 4.0) in carbon-coated quartz tubes (Ø ≈ 20 mm) in an N_2-filled glovebox. The tubes were sealed under vacuum (∼10^{-4} Torr) and slowly heated to 723 K in 12 h, then to 1423 K in 7 h, soaked at this temperature for 6 h, and subsequently water quenched to room temperature. The obtained ingots were crushed into powders and then densified by the spark plasma sintering (SPS) method (SPS-10-4, Thermal Technology). To prepare for SPS processing, the melt grown ingots were ground to a powder using a mortar and pestle to reduce the grain size to smaller than 5 mm^3 and then further ground by a mechanical mortar and pestle to reduce the grains to less than 53 μm^3. These powders were then densified at 723 K for 10 min in a 20 mm diameter graphite die under an axial compressive stress of 60 MPa in an argon atmosphere. Highly dense disk-shaped pellets with dimensions of Ø 20 mm × 9 mm were obtained. The manipulations and preparative steps for the Na-doped PbS, SrS, CaS starting materials, and the grinding powders for SPS, were carried out in a purified Ar−atmosphere glovebox, with total O_2 and H_2O level <0.1 ppm. The obtained samples were sealed inside an evacuated quartz tube with a pressure of ∼10^{-4} Torr and annealed at 723 K for 15 d to evaluate their thermal stability (typical annealed samples in this study are shown in Figure S1 of the Supporting Information).

Physical Characterization. *Electrical Properties.* The obtained SPS processed pellets were cut into bars with dimensions 15 mm × 3 mm × 3 mm that were used for simultaneous measurement of the Seebeck coefficient and the electrical conductivity using an Ulvac Riko ZEM-3 instrument under a helium atmosphere from room temperature to 923 K. The samples were coated with a thin (∼0.1−0.2 mm) layer of boron nitride (BN) to protect instruments (see the Supporting Information for sample photographs of different preparation stages, Figure S2). Heating and cooling cycles gave repeatable electrical properties. Electrical properties obtained from different slices cut from the same pellets were similar, attesting to the homogeneity of the samples. The uncertainty of the Seebeck coefficient and electrical conductivity measurements is 5%.

Hall Measurements. The Hall coefficient was measured with a homemade high temperature apparatus, which provides a working range from 300 to 723 K. The sample was press mounted and protected with argon gas to avoid possible oxidation at high temperature. The Hall resistance was monitored with a Linear Research AC Resistance Bridge (LR-700), with constant magnetic fields of ±1 T applied by using an Oxford Superconducting Magnet.

Thermal Conductivity. High density SPS processed pellets were cut and polished into coins of Ø ≈ 8 mm and 1−2 mm thickness for thermal diffusivity measurements. The samples were coated with a thin layer of graphite to minimize errors from the emissivity of the material. The thermal conductivity was calculated from $k = D \cdot C_p \cdot \rho$, where the thermal diffusivity coefficient (D) was measured using the laser flash diffusivity method in a Netzsch LFA457, the specific heat capacity (C_p) was indirectly derived using a representative sample (Pyroceram 9606) in the range 300−923 K, and the density (ρ) was determined using the dimensions and mass of the sample, which was then reconfirmed using

dx.doi.org/10.1021/ja301772w | J. Am. Chem. Soc. 2012, 134, 7902−7912

gas pycnometer (Micromeritics AccuPyc1340) measurements. The thermal diffusivity data were analyzed using a Cowan model with pulse correction,[20,21] and heating and cooling cycles give reproducible values for each sample. The C_p results show good agreement with the reported values.[26] Thermal diffusivities obtained for different slices from the same pellet are also similar. The uncertainty of the thermal conductivity is estimated to be within 8%, considering the uncertainties for D, C_p, and ρ. The thermal diffusion and the heat capacity data for all samples can be found in the Supporting Information (Figures S3, S5, S7, and S9). The combined uncertainty for all measurements involved in the calculation of ZT is less than 15%. No directional anisotropy effects were observed in the charge transport properties.

Electron Microscopy and X-ray Diffraction. Transmission electron microscopy (TEM) investigations were carried out in a JEOL 2100F microscope operated at 200 kV. The thin TEM specimens were prepared by conventional methods and include cutting, grinding, dimpling, polishing, and Ar-ion milling on a liquid nitrogen cooling stage. Samples pulverized with an agate mortar were used for powder X-ray diffraction. The powder diffraction patterns were obtained with Cu K_α (λ = 1.5418 Å) radiation in a reflection geometry on an Inel diffractometer operating at 40 kV and 20 mA and equipped with a position-sensitive detector.

RESULTS AND DISCUSSION

The strategy for improving the thermoelectric performance of p-type PbS via Na doping and SrS and CaS nanostructuring is described below in several successive steps. First, the electrical transport properties (power factor) of PbS were optimized through Na doping. Second, we chose SrS and CaS as second phases and varied their fraction in the Na optimized PbS. We show that a high ZT is obtained through the combination of high power factor and low thermal conductivity achieved by optimized Na doping and nanostructuring, respectively. Third, thermoelectric measurements up to 923 K for the samples with optimized compositions coated with a thin layer of boron nitride (BN) were carried out to demonstrate the continued rise in ZT with no sign of saturation. Finally, a 15 d annealing treatment of optimized samples is presented and shows a slight improvement of the thermoelectric properties, suggesting excellent thermal stability.

1. PbS Doped with *x*% Na. Na was chosen as the dopant to tune the hole carrier concentration by substituting Na^+ for Pb^{2+} to optimize the electrical transport properties for the PbS matrix. As shown in Figure 1a, all of the PXRD patterns can be indexed to the NaCl structure type as a single PbS phase. Figure 1b shows a typical SPS disk-shaped pellet used in this study. The density of these pellets is ~97% of the theoretical density. As shown in Figure 1c, the lattice parameter decreases with increasing Na concentration, consistent with the smaller radius of Na^+ ions (~0.97 Å) as compared to that of Pb^{2+} ions (~1.20 Å). Also, the Hall carrier concentrations (n_H) at room temperature increase rapidly from 0.40×10^{19} cm^{-3} for pure PbS to 8.27×10^{19} cm^{-3} for the sample with 4.0% Na doping. Collectively, the lattice parameter variation and increased carrier concentrations indicate that Na^+ was successfully incorporated into the PbS lattice.

Figure 2 shows the thermoelectric properties as a function of temperature for PbS doped with *x*% Na. The electrical conductivity decreases with rising temperature, as shown in Figure 2a. As the content of Na rises, the room-temperature electrical conductivity significantly increases from ~102 S cm^{-1} for pure PbS to ~2209 S cm^{-1} for the sample with 4.0% Na doping. The increase in electrical conductivity mainly results from the greater charge carrier concentration. There is also

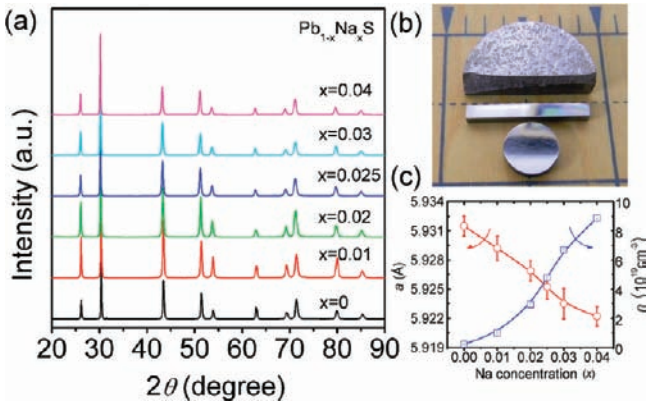

Figure 1. (a) Powder XRD patterns for PbS with *x*% Na doping; (b) typical SPS disk-shaped pellet and samples used in this study; and (c) the lattice parameters and carrier density as a function of Na concentration; the error bars for carrier density are smaller than the symbol size.

good agreement between the trend in the measured Hall carrier concentrations listed in Table 2 and the room-temperature electrical conductivity.

As shown in Figure 2b, the Seebeck coefficients are negative for pure PbS and rapidly change sign upon Na doping, indicating a strong tendency of conversion from electron-dominated transport to hole-dominated transport. The Seebeck coefficient at room temperature for pure PbS is about −240 μV K^{-1}. As Na is added, the room-temperature Seebeck coefficient becomes positive and then decreases with increasing Na; the Seebeck coefficient varies from about +140 μV K^{-1} for the sample with 1.0% Na doping to +46 μV K^{-1} for the sample with 4.0% Na doping.

The power factor of pure PbS shows a maximum value of ~6.0 μW cm^{-1} K^{-2} around room temperature, which falls to ~5.0 μW cm^{-1} K^{-2} at 723 K, Figure 2c. The maximum of the power factor shifts to higher temperature as the amount of Na is increased. The power factor peaks at ~9.0 μW cm^{-1} K^{-2} at 723 K in the 2.5% Na-doped sample, and then decreases slightly to ~8.2 μW cm^{-1} K^{-2} at 723 K as the Na doping content rises to 4.0%.

The total thermal conductivity as a function of temperature for the different levels of Na doping is shown in Figure 2d. (Heat capacity and thermal diffusivity for Na doped PbS can be found in the Supporting Information, Figures S3a and b). The total thermal conductivity (κ_{tot}) is essentially the sum of the electronic (κ_{ele}) and lattice thermal conductivity (κ_{lat}). Generally, κ_{lat} can be estimated by subtracting κ_{ele} from κ_{tot}. The electronic part (κ_{ele}) is proportional to the electrical conductivity (σ) through the Wiedemann−Franz relation, $\kappa_{ele} = L\sigma T$, where L is the Lorenz number.[27] Because nanostructuring has proved to be an effective method for reducing the lattice thermal conductivity κ_{lat},[1] separating the electronic and lattice parts is important in studying the effect of embedded nanostructures in a host thermoelectric matrix.

The Lorenz numbers of 1.5×10^{-8} W Ω K^{-2} (nondegenerate limit) and 2.45×10^{-8} W Ω K^{-2} (degenerate limit) do not hold true for nondegenerate or heavily doped semiconductors, where a large change in the chemical potential is observed with temperature.[25] Here, the Lorenz number was obtained by applying the calculated reduced Fermi energy (η) and scattering parameter (r) assuming a single band model.[17,20,21,28] The single band model is supported by the

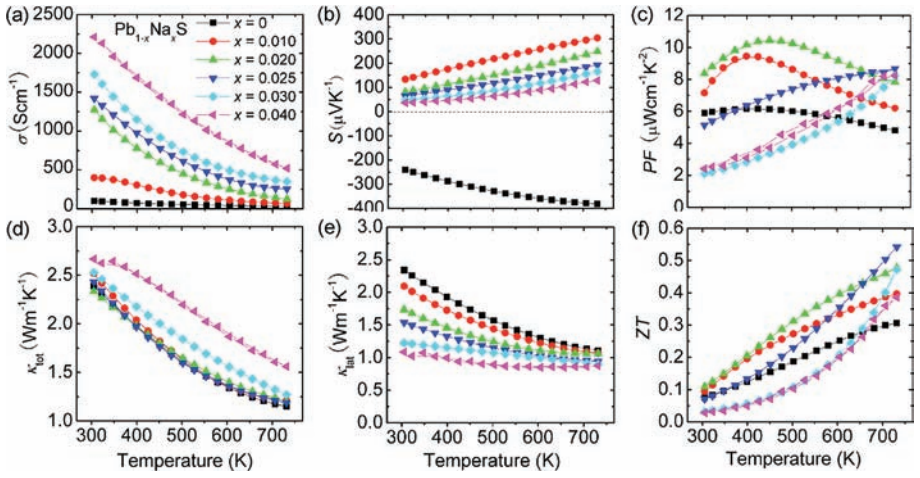

Figure 2. Thermoelectric properties as a function of temperature for PbS with *x*% Na doping: (a) electrical conductivity; (b) Seebeck coefficient; (c) power factor; (d) total thermal conductivity; (e) lattice thermal conductivity; and (f) figure of merit, *ZT*.

Table 2. Transport Properties of PbS-Based Polycrystallines[a]

samples	n_H (10^{19} cm^{-3})	r_H	μ_H (cm^2 V^{-1} s^{-1})	S (μV K^{-1})	σ (S cm^{-1})	$m^*(m_o)$	κ_L (RT) (W m^{-1} K^{-1})	κ_L (723 K) (W m^{-1} K^{-1})	ZT_{max} (723 K)
PbS	0.40	1.16	277	−240	102	0.38	2.34	1.11	0.31
$Pb_{0.990}Na_{0.010}S$	1.00	1.11	251	140	402	0.37	2.09	1.07	0.40
$Pb_{0.980}Na_{0.020}S$	2.95	1.06	270	81	1274	0.39	1.73	1.06	0.48
$Pb_{0.975}Na_{0.025}S$	4.78	1.04	186	65	1421	0.42	1.54	0.94	0.54
$Pb_{0.970}Na_{0.030}S$	6.69	1.03	162	54	1729	0.39	1.22	0.89	0.47
$Pb_{0.960}Na_{0.040}S$	8.27	1.02	156	46	2209	0.35	1.09	0.87	0.39
$Pb_{0.975}Na_{0.025}S$+1.0% SrS	5.17	1.04	125	69	1037	0.48	1.30	0.83	0.60
$Pb_{0.975}Na_{0.025}S$+2.0% SrS	5.01	1.04	120	67	960	0.46	1.39	0.73	0.63
$Pb_{0.975}Na_{0.025}S$+3.0% SrS	4.55	1.05	93	73	678	0.47	1.19	0.64	0.73
$Pb_{0.975}Na_{0.025}S$+4.0% SrS	4.72	1.05	62	71	467	0.47	1.09	0.55	0.60
$Pb_{0.975}Na_{0.025}S$+1.0% CaS	5.02	1.05	123	66	990	0.45	1.47	0.79	0.51
$Pb_{0.975}Na_{0.025}S$+2.0% CaS	4.95	1.04	109	65	866	0.44	1.24	0.74	0.62
$Pb_{0.975}Na_{0.025}S$+3.0% CaS	4.81	1.06	97	78	743	0.52	1.12	0.69	0.72
$Pb_{0.975}Na_{0.025}S$+4.0% CaS	4.70	1.06	67	81	503	0.51	0.83	0.55	0.66

[a] n_H, carrier concentration; r_H, Hall factor; μ_H, carrier mobility; S, Seebeck coefficient; σ, electrical conductivity; $m^*(m_o)$, the effective mass; κ_L, lattice thermal conductivity; ZT, the dimensionless figure of merit.

high temperature Hall effect data presented below. The Fermi energy can be derived from the measured Seebeck coefficients, assuming that acoustic phonon scattering is the main carrier scattering mechanisms ($r = -1/2$). (Lorenz number for PbS with *x*% Na doping, Figure S3c, and the calculated details can be found in the Supporting Information.) It is readily apparent from Figure S3d (Supporting Information) that the increase of the total thermal conductivity (κ_{tot}) as the Na doping content exceeds 2.5% is a result of the increasing contribution from the electronic thermal conductivity (κ_{ele}).

After proper calculation of κ_{ele}, we observe that the lattice thermal conductivity decreases with both increasing temperature and increasing Na doping; see Figure 2e. This is significantly different from the behavior of lattice thermal conductivity in n-type PbS, in which the lattice thermal conductivity exhibits a negligible change with variations in the $PbCl_2$ dopant.[21] A TEM study reveals PbS doped with 2.5% Na is a quasi-solid solution; that is to say, we can see the homogeneous distribution of all elements in the sample, except for some Na-rich precipitates at grain boundaries. The low magnification TEM image of the 2.5% Na doped sample is shown in Figure 3a. The grains with an average size of 1.0 μm resulting from the SPS processing are easily observed, and the contrast within them is very uniform. However, some dark spots can be detected at the grain boundaries, as shown in the inset scanning transmission electron microscopy (STEM) image.

The high-resolution TEM image in Figure 3b further confirms our observation; that is, the interior of the grains is very "clean" and does not show any nanostructures. The inset electron diffraction pattern along the [011] direction, collected with a large aperture, shows that the PbS structure (i.e., crystal symmetry) is not changed by Na doping. Energy dispersive X-ray spectroscopy (EDS) spectra in STEM mode using a 1.0 nm

dx.doi.org/10.1021/ja301772w | J. Am. Chem. Soc. 2012, 134, 7902−7912

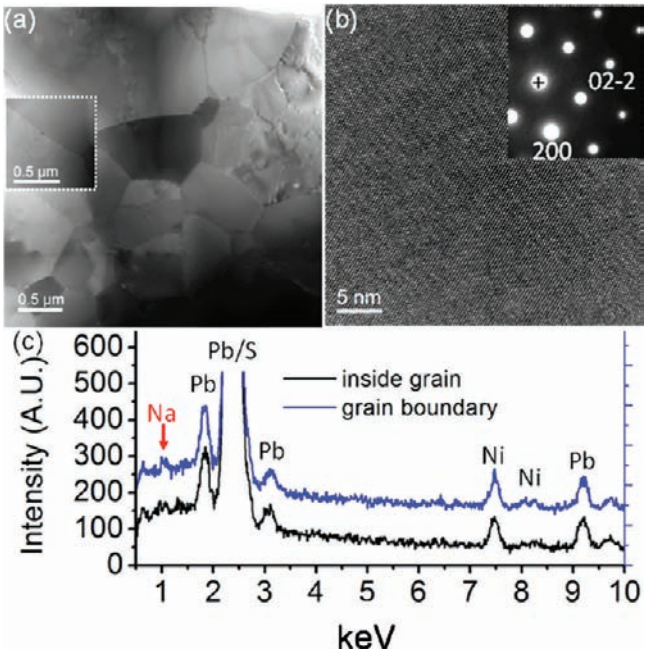

Figure 3. (a) Low magnification TEM image of $Pb_{0.975}Na_{0.025}S$ showing many grains with average size around 1.0 μm; an STEM image (inset) reveals one clear grain boundary. (b) High-resolution TEM image showing no nanostructures inside the grain; inset: the corresponding diffraction pattern along [011] direction, showing a single phase. (c) EDS spectra from inside grain and grain boundary both having Na signal.

probe size were also recorded and are shown in Figure 3c. The blue spectrum is from a typical grain boundary, and the black was obtained from the inside of one randomly selected grain. Both spectra clearly show Na peaks in the region around 1.0 keV, and the peak intensity in the boundary is only slightly higher than that in the grain itself. This observation provides evidence that the sample contains only a very small fraction of Na in the form of Na-rich precipitates at grain boundaries, while the majority contributes carriers to the sample. Therefore, the reduction in lattice thermal conductivity for Na-doped PbS is mostly attributed to the point defects of Na in the PbS lattice. This can be explained by the Callaway model[29] for solid solution alloys if the Na concentration matches the solubility limit. The Callaway model assumes that the scattering arises by point defects and Umklapp processes alone[29] and generally does well describing the lattice thermal conductivity of solid solution systems. The point defects enhance phonon scattering because of mass fluctuations (mass differences) and strain fluctuations (size differences) between the guest atom and those of the host lattice.[30−32] However, it would be worth pointing out that the reduction in lattice thermal conductivity by Na doping is less pronounced at high temperature (>700 K), and this is because the Umklapp scattering dominates over point defect scattering.

The guest atoms in the host lattice in both n- and p-type PbS are Cl^- and Na^+, respectively. The size difference between Na^+ and Pb^{2+} is ~0.23 Å (Na^+ ~0.97 Å, Pb^{2+} ~1.20 Å), which is much larger than the difference between S^{2-} and Cl^- (S^{2-} ~1.84 Å, Cl^- ~1.81 Å). Also, the mass difference between Na and Pb is ~184.21 au (Na ~22.99, Pb ~207.2), which is again much larger than that between S and Cl (S ~32.06, Cl ~35.45). Therefore, it can be easily understood why the lattice thermal conductivity is insensitive to $PbCl_2$ doping[21] but highly dependent upon Na doping. Combining the results of the electrical and thermal transport properties, a maximum *ZT* value of 0.54 was obtained for the optimally doped 2.5% Na sample, Figure 2f. This doping level was then used for the subsequent nanostructuring studies and thermoelectric optimization presented below.

2. Samples of $Pb_{0.975}Na_{0.025}S$ with *x*% SrS and CaS. The thermoelectric properties of PbS with varying amounts of SrS and CaS were evaluated at a fixed Na concentration of 2.5%, which was shown above to maximize the power factor and *ZT*. For the SrS containing samples, the PXRD patterns show a single phase that can be indexed to the NaCl structure type regardless of the amount of added SrS (up to 4.0%), Figure S4 (Supporting Information). The electrical conductivities decrease with increasing temperature and are lower for increasing amounts of SrS over the entire temperature range (Figure 4a); however, the Seebeck coefficients show negligible changes (Figure 4b). This suggests the carrier concentration, controlled by the Na concentration, is similar for all samples, and the rising fraction of SrS as a second phase diminishes the hole mobility, Table 2. As shown in Figure 4c, the power factors for

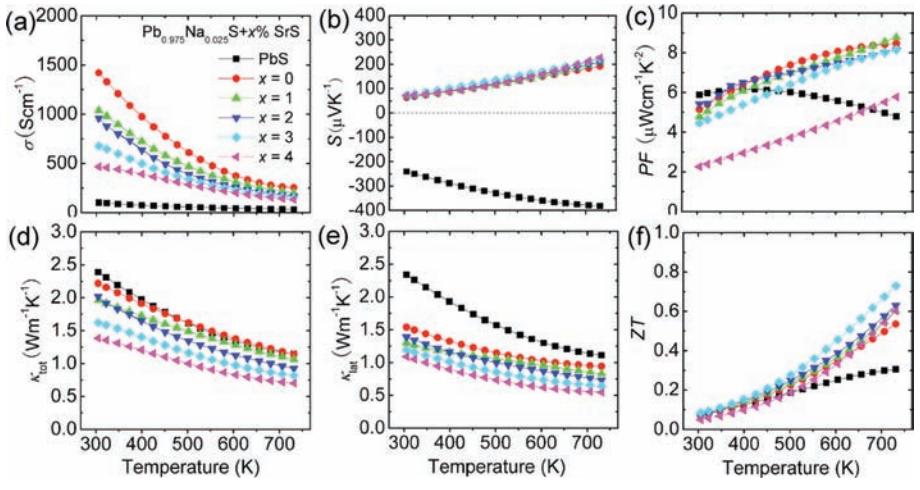

Figure 4. Thermoelectric properties as a function of temperature for $Pb_{0.975}Na_{0.025}S$ with different SrS contents: (a) electrical conductivity; (b) Seebeck coefficient; (c) power factor; (d) total thermal conductivity; (e) lattice thermal conductivity; and (f) figure of merit, *ZT*.

dx.doi.org/10.1021/ja301772w | J. Am. Chem. Soc. 2012, 134, 7902−7912

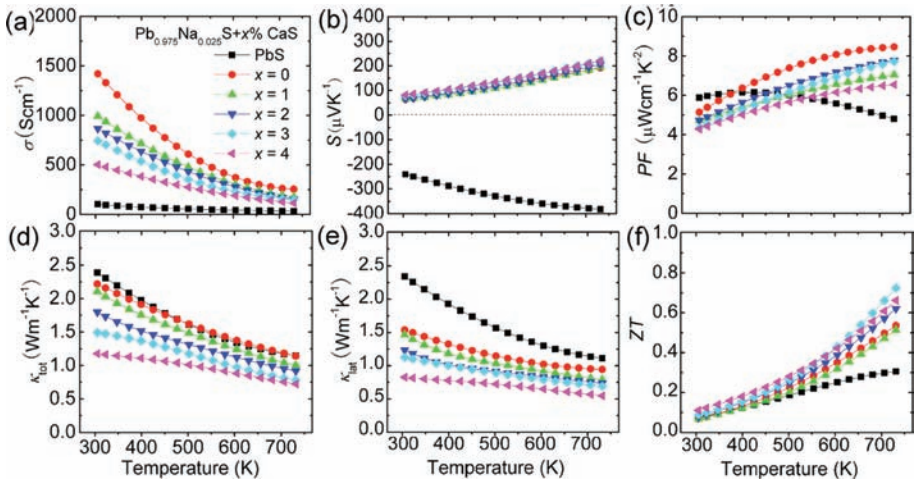

Figure 5. Thermoelectric properties as a function of temperature for $Pb_{0.975}Na_{0.025}S$ with different CaS contents: (a) electrical conductivity; (b) Seebeck coefficient; (c) power factor; (d) total thermal conductivity; (e) lattice thermal conductivity; and (f) figure of merit, *ZT*.

all samples peak at 723 K. As compared to $Pb_{0.975}Na_{0.025}S$, the samples containing 1.0−3.0% SrS show only a small reduction in electrical conductivity at 723 K and nearly no change in Seebeck coefficient, resulting in a similar power factor ranging from ∼8.2 to ∼8.8 μW cm^{-1} K^{-2} at 723 K.

The total thermal conductivity of samples with SrS as a second phase shows a significant decrease with increasing SrS (Figure 4d). (Heat capacity, thermal diffusivity, Lorenz number, and electronic thermal conductivity for $Pb_{0.975}Na_{0.025}S$ with varying amounts of SrS are given in the Supporting Information, Figure S5). This falling trend is also observed in the lattice thermal conductivity (Figure 4e), indicating that the dispersed SrS phase is highly effective in reducing the lattice thermal conductivity. At room temperature, the lattice thermal conductivity significantly decreases from ∼2.34 W m^{-1} K^{-1} for pure PbS to ∼1.30 W m^{-1} K^{-1} for the Na doped sample with 1.0% SrS, which further decreases to ∼1.09 W m^{-1} K^{-1} as the SrS content is increased to 4.0%. Correspondingly, the lattice thermal conductivity at 723 K decreases from ∼1.11 W m^{-1} K^{-1} for pure PbS to ∼0.83 and ∼0.55 W m^{-1} K^{-1} for the 1.0% and 4.0% SrS samples, respectively.

As shown in Figure 4f, the maximum *ZT* value of ∼0.73 at 723 K is observed for the $Pb_{0.975}Na_{0.025}S$ sample with 3.0% SrS and shows no sign of saturation at higher temperatures. This value is 35% higher than the highest *ZT* value of 0.54 for the 2.5% Na-doped PbS sample with no SrS. The experimental results indicate that the introduction of 3.0% SrS significantly boosts the thermoelectric properties of p-type PbS.

CaS was selected as another candidate to investigate whether the relative size of the metals (e.g., Sr vs Ca) as compared to that of Pb had a marked effect on the thermoelectric properties of PbS, in particular on the lattice thermal conductivity. The PXRD patterns of $Pb_{0.975}Na_{0.025}S$ with varying amounts of CaS show a single phase that can be indexed to the NaCl structure type regardless of CaS concentration (up to 4.0%), as shown in Figure S6 (Supporting Information) (heat capacity, thermal diffusivity, Lorenz number, and electronic thermal conductivity for these samples can be found in the Supporting Information, Figure S7). The results show that all electrical and thermal transport behavior, Figure 5, for the $Pb_{0.975}Na_{0.025}S$ samples with CaS as the second phase is very similar to that of SrS. The CaS containing samples reach a maximum *ZT* value of 0.72 for the $Pb_{0.975}Na_{0.025}S$ sample with 3.0% CaS.

The Seebeck coefficients of the Na-doped samples with and without the added metal sulfide phases were checked as a function of carrier concentration at room temperature. The well-established Pisarenko relation of the Seebeck coefficient and carrier concentration, assuming a parabolic band and an acoustic phonon scattering mechanism, give a good description of the experimental data. In this approximation, the carrier concentration (n) and Seebeck coefficient (S) were approximated by the relationships:[17,20,21]

$$n = 4\pi\left(\frac{2m^* k_B T}{h^2}\right)^{3/2} \frac{F_{1/2}(\eta)}{r_H} \quad (1)$$

$$S = \pm\frac{k_B}{e}\left(\frac{(r+5/2)F_{r+3/2}(\eta)}{(r+3/2)F_{r+1/2}(\eta)} - \eta\right) \quad (2)$$

In the above equations, η is the reduced Fermi energy, $F_n(\eta)$ is the nth order Fermi integral, k_B is the Boltzmann constant, m^* is the effective mass, h is the Planck constant, e is the electron charge, and r is the scattering factor. Here, it should be noted that the Hall coefficient, r_H, which takes into account band anisotropy and the relaxation time of carriers moving along and across the principal conduction axis of the Fermi surface, will be about unity for parabolic bands and a spherical Fermi surface.[33] The scattering factor (r) is −1/2 because acoustic phonon scattering has been assumed as the main carrier scattering mechanism near room temperature.[34]

Using eqs 1 and 2, we varied the values of the reduced Fermi energy to generate carrier concentration (n) and Seebeck coefficient (S) pairs for pure PbS with varied effective masses of 0.25−0.50 m_o. The results are shown as lines in Figure 6 and compared to several PbS samples with x% Na doping. The carrier concentration increases from 0.40 × 10^{19} cm^{-3} for pure PbS to 1.00 × 10^{19}, 2.95 × 10^{19}, 4.78 × 10^{19}, 6.69 × 10^{19}, and 8.27 × 10^{19} cm^{-3} as the doping percentages increase to 1.0, 2.0, 2.5, 3.0, and 4.0, respectively. It is noteworthy that the Seebeck coefficients for the $Pb_{0.975}Na_{0.025}S$ samples with 1.0% and 4.0% SrS or CaS agree with pure PbS within the studied carrier concentration range. It is evident from Figure 6 that a parabolic band dominated by acoustic phonon scattering with an effective charge carrier mass of $m^* \approx 0.4\ m_o$ describes the experimental data rather well. The experimentally determined values and the Pisarenko lines show excellent agreement, suggesting that the

dx.doi.org/10.1021/ja301772w | J. Am. Chem. Soc. 2012, 134, 7902−7912

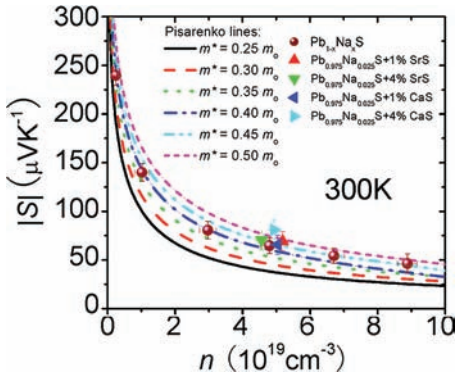

Figure 6. Pisarenko plots at 300 K. Seebeck coefficients as a function of carrier concentration. The lines correspond to the theoretically expected curves for the pristine PbS with $m^* \approx xm_o$ (x = 0.25, 0.30, 0.35, 0.40, 0.45, and 0.50). The excellent agreement suggests that Na doping levels and second phases (SrS/CaS) have no marked effects in perturbing the electronic density of states of PbS.

carrier scattering mechanism is not greatly affected by Na doping or the nanostructuring second phases (SrS/CaS), as well as no particular enhancement of the Seebeck coefficient by resonant scattering. Consequently, a marked effect of doping on the density of states of the PbS matrix is ruled out in this work. Therefore, it can be concluded that the modest thermoelectric properties of p-type PbS are greatly enhanced by optimizing the power factor through tuning the carrier concentration across the valence band (occurring at the L point of the Brillouin zone)[35] and by vastly reducing the lattice thermal conductivity through nanostructuring with appropriate second phases.

The Role of the Second Valence Band in PbS. It is well-known for PbTe that the first valence band at the L point of the Brillouin zone and a second valence band near the Σ point, also known as the heavy hole band, play a significant role in the charge transport and thermoelectric properties of heavily doped PbTe.[13,15,33,36] As the temperature rises well above 500 K, this heavy hole band contributes thermally excited heavy holes, and the transport is dominated by two bands rather than one. This manifests itself as a substantial enhancement in the Seebeck coefficient (through enhancement of the effective mass (m^*)) and an apparent rise in the carrier concentration at high temperature. It is the key factor for the high ZT values obtained in p-type PbTe.[33] The question then arises whether a similar effect is at work in the case of PbS. Electronic band structure calculations indicate that a second valence band near the Σ point does exist in PbS but it lies at a much lower energy.[37]

Our high temperature Seebeck and Hall coefficient data are consistent with a single band model. For example, no particular enhancement of the Seebeck coefficient is observed at high temperature in p-type PbS with heavy Na doping. The effects of the heavy valence band can usually be observed at a higher carrier concentration (3×10^{19} cm^{-3} for p-type PbTe),[13,15,33,36] resulting in Hall coefficient (R_H) peaks as a function of temperature at ~500 K. To check for the presence of a "heavy valence band" in p-type PbS, three samples with heavy carrier concentrations were prepared, that is, 8.1×10^{19}, 11×10^{19}, and 30×10^{19} cm^{-3}, as shown in Figure S8. Two PbTe samples with carrier concentrations of 5.5×10^{19} and 10×10^{19} cm^{-3} are also plotted for comparison. Contrary to the PbS samples, both PbTe samples show R_H peaks above 400 K. For the PbS samples, the Hall coefficients (R_H) are almost independent of temperature and no R_H peaks are observed, which is consistent with no heavy valence band contribution in p-type PbS.

Transmission Electron Microscopy. Samples of $Pb_{0.975}Na_{0.025}S$ with 3.0% SrS or CaS were investigated by TEM in detail (Figures 7–9). Figure 7a is a representative low

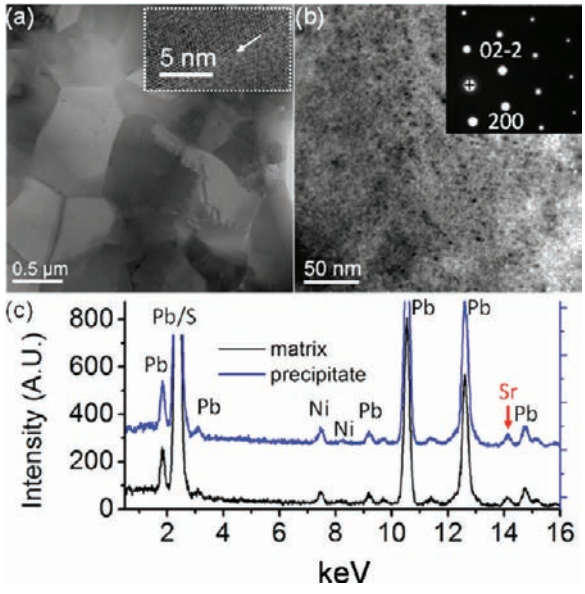

Figure 7. (a) Low magnification TEM image of $Pb_{0.975}Na_{0.025}S$ with 3.0% SrS; inset shows a high-resolution TEM image of one grain boundary. (b) Middle magnification TEM image showing high number density nanostructures inside one grain; inset: the corresponding diffraction pattern along [011] direction shows all spots from PbS matrix. (c) EDS spectra from matrix and precipitate both showing Sr signal.

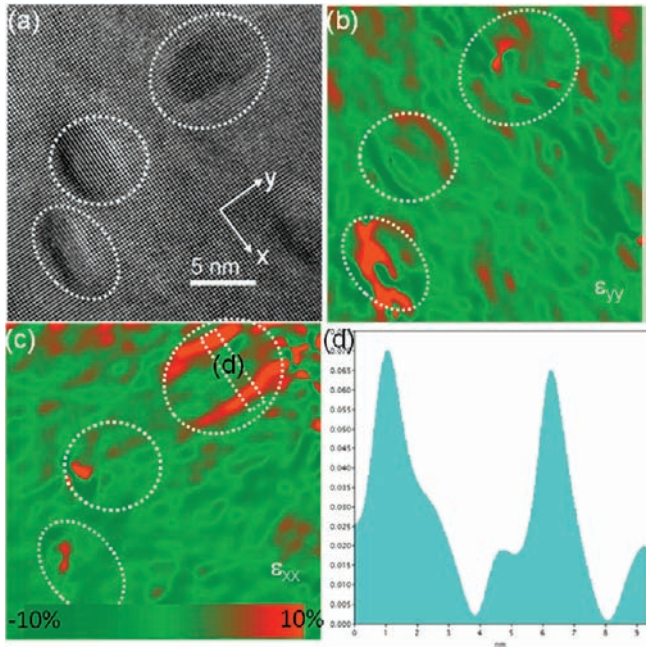

Figure 8. (a) High magnification TEM image of $Pb_{0.975}Na_{0.025}S$ with 3.0% SrS sample, which confirms crystallographic alignment between PbS and SrS. (b) and (c) are the ε_{yy} and ε_{xx} strain maps of the images in (a), respectively. The color bar indicates −10% to 10% strains. (d) The line scanning profile of the marked region in (c), showing the 6% difference of lattice parameter at the interface between PbS and SrS.

dx.doi.org/10.1021/ja301772w | J. Am. Chem. Soc. 2012, 134, 7902–7912

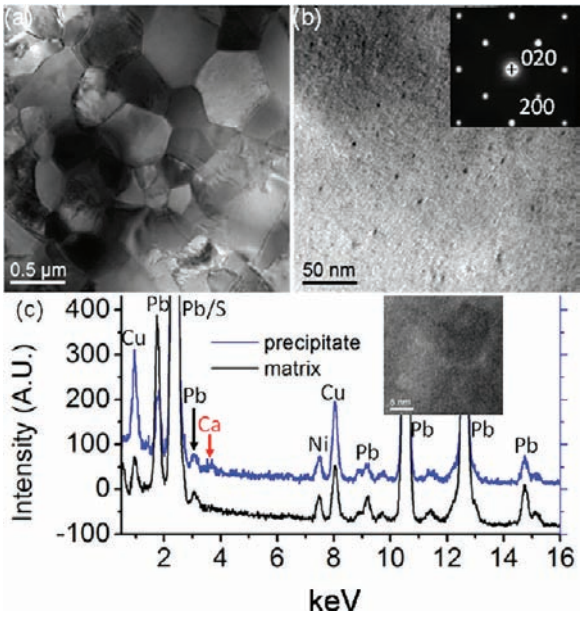

Figure 9. (a) Low magnification TEM image of $Pb_{0.975}Na_{0.025}S$ with 3.0% CaS. (b) Middle magnification TEM image showing a low number density of nanostructures inside one grain; inset: the corresponding diffraction pattern along [001] direction does not show any spot splitting. (c) EDS spectra from matrix and precipitate; the corresponding TEM image is shown as the inset.

magnification TEM image of $Pb_{0.975}Na_{0.025}S$ with 3.0% SrS, which clearly shows grain boundary contrast due to incoherence between most grains and as shown in the high-resolution TEM image (inset). The average grain size is about 0.8 μm. The high-resolution TEM image inside a single grain reveals a high number density of nanostructures, shown as dark spots in Figure 7b. The inset electron diffraction pattern from both the matrix and the precipitates shows Bragg spots only from PbS, indicating an endotaxial relationship between the PbS and SrS lattices. The EDS spectra of the matrix (black) and precipitate (blue) show a Sr peak around 14 keV. EDS analysis also shows that the Sr peak intensity of precipitate is higher than that of matrix, indicating that the precipitate is SrS and some additional Sr dissolves in PbS to form a solid solution. The solubility limit of SrS in PbS is ~1.0% based on our TEM observations.

Figure 8a shows a typical lattice image with an average precipitate size of ~4 nm in the $Pb_{0.975}Na_{0.025}S$ with 3.0% SrS sample. To determine the possible presence of elastic and plastic strain, the image in Figure 8a was subjected to geometric phase analysis (GPA).[38,39] GPA is a lattice image processing method for semiquantitative spatially distributed strain field analysis and was used to investigate the variation in the lattice parameter, and thus the strain, at/around boundaries. Figure 8b and c shows the ε_{yy} and ε_{xx} strain map profiles of the precipitates, respectively. From the strain map distribution of this image, it appears that elastic strain is pervasive in and around the precipitates. The line scanning profile of the marked region in Figure 8c at the PbS/SrS interface along the x direction in Figure 7a shows a maximum 6% difference in lattice parameter between the two phases.

Figure 9a is another typical low magnification TEM image of $Pb_{0.975}Na_{0.025}S$ with 3.0% CaS, which clearly shows smaller average grain sizes (~0.4−0.5 μm) than either $Pb_{0.975}Na_{0.025}S$ or $Pb_{0.975}Na_{0.025}S$ with 3.0% SrS. As compared to the sample containing 3.0% SrS, we surprisingly find a very low number density of nanostructures in the 3.0% CaS sample; see Figure 9b. The EDS spectra of the matrix (black) and precipitate (blue) recorded in the region marked in the inset image are shown in Figure 9c. We can see the small Ca peak in both the matrix and the precipitate, which means Ca is distributed throughout the sample. The TEM results also suggest a higher solubility limit of Ca in PbS for the 3% sample, which is estimated to be ~2.5%.

The TEM results indicate that both SrS and CaS containing samples show nanoprecipitates as well as solubility of the second phase in the PbS matrix; therefore, the lattice thermal conductivity would be affected by both nanostructures as well as point defects created by the solid solution. To understand the role of the nanostructures and point defects in reducing the lattice thermal conductivity of $Pb_{0.975}Na_{0.025}S$ with 3.0% SrS/CaS, we performed theoretical calculations of the lattice thermal conductivity based on the modified Callaway model.[29,30] The lattice thermal conductivity is given by:

$$\kappa_{lat} = \frac{k_B}{2\pi^2 v}\left(\frac{k_B T}{\hbar}\right)^3 \int_0^{\theta_D/T} \tau_c \frac{x^4 e^x}{(e^x - 1)^2} dx \quad (3)$$

where k_B is the Boltzmann constant, $\hbar$ is the reduced Plank constant, T and θ_D are the absolute and the Debye temperatures, respectively, v is an average phonon-group velocity, $x = \hbar\omega/\kappa_B T$, τ_N is the relaxation time due to normal phonon−phonon scattering, and τ_c is the combined relaxation time. The latter (τ_c) is obtained by integrating the relaxation times from various processes, and most of the parameters are taken from He et al.[40] On the basis of our TEM studies, for a certain frequency, the relaxation time depends mainly on scattering from the nanoscale precipitates, dislocations, boundaries, and the phonon−phonon interactions. The overall relaxation time is then:

$$\tau_c^{-1} = \tau_U^{-1} + \tau_N^{-1} + \tau_{PD}^{-1} + \tau_B^{-1} + \tau_S^{-1} + \tau_P^{-1} \quad (4)$$

where τ_U, τ_N, τ_{PD}, τ_B, τ_S, and τ_P are the relaxation times corresponding to scattering from Umklapp processes, normal processes, point defects due to solid solution, boundaries, strain, and precipitates, respectively.[40] On the basis of these formulas and the parameters obtained from the TEM observations and He et al.,[40] we have calculated the lattice thermal conductivity of pure PbS, $Pb_{0.975}Na_{0.025}S$, and $Pb_{0.975}Na_{0.025}S$ with 3.0% SrS and CaS. The results are shown in Figure 10a. Similar to the calculation of PbTe,[40] we fitted our

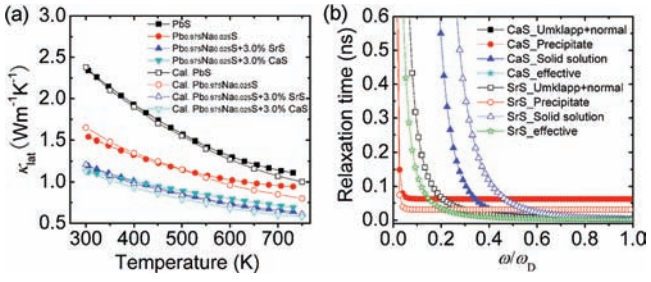

Figure 10. (a) Temperature dependence of calculated and experimental lattice thermal conductivity of PbS and $Pb_{0.975}Na_{0.025}S$, $Pb_{0.975}Na_{0.025}S$ with 3.0% SrS/CaS samples. (b) Relaxation time versus the normalized frequency for $Pb_{0.975}Na_{0.025}S$ with 3.0% SrS/CaS samples at 300 K. The phonon frequency (ω) is normalized to the Debye frequency (ω_D).

dx.doi.org/10.1021/ja301772w | J. Am. Chem. Soc. 2012, 134, 7902−7912

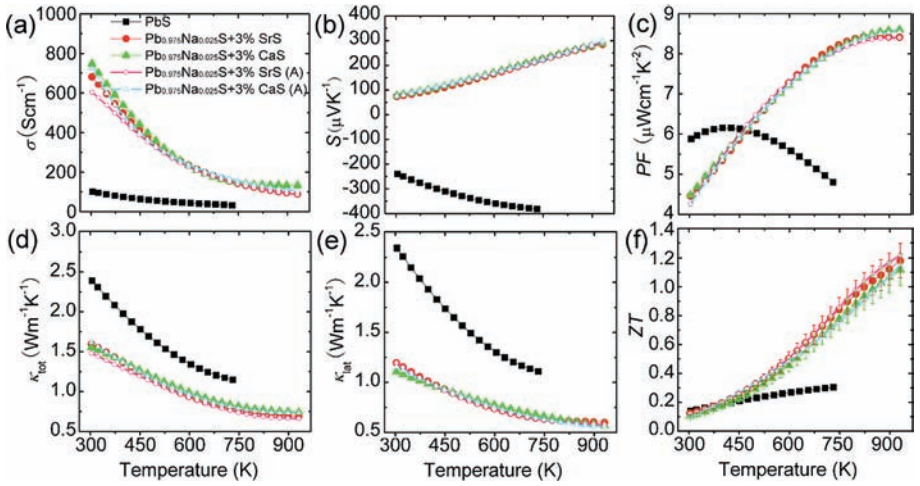

Figure 11. Thermoelectric properties up to 923 K as a function of temperature for $Pb_{0.975}Na_{0.025}S$ with 3.0% SrS/CaS with and without annealing treatment: (a) electrical conductivity; (b) Seebeck coefficient; (c) power factor; (d) total thermal conductivity; (e) lattice thermal conductivity; and (f) figure of merit, *ZT*. "A" represents the samples annealed at 723 K for 15 d.

calculated data to the experimental by adjusting the contribution of normal phonon−phonon scattering. All other calculations based on TEM observations match the experimental data reasonably well. For the $Pb_{0.975}Na_{0.025}S$ with 3.0% SrS/CaS samples, the plots of relaxation times based on theoretical data for some of the above possible contributing terms are shown in Figure 10b. It indicates that both nanoscale precipitates and point defects play an important role in reducing the lattice thermal conductivity, but the contribution from nanoscale precipitates contained in a sample with SrS is larger than that in sample with CaS. Figure 10b further reveals that nanoscale precipitates scatter both middle and high frequency phonons, whereas a solid solution (point defect scattering) mainly affects the latter.

3. Absence of Thermoelectric Property Saturation Up to 923 K for $Pb_{0.975}Na_{0.025}S$ with 3.0% SrS (CaS). The results presented above show that the *ZT* values for all samples have an increasing trend with temperature with no sign of saturation in the Seebeck coefficient. This indicates the absence of significant bipolar diffusion up to 723 K, which is also confirmed by the temperature dependence of the thermal conductivity presented above. Because the energy band gap for lead chalcogenides shows a well-known anomalous increase with temperature,[41,42] we can expect the band gap of PbS to be significantly larger than 0.41 eV[20] at elevated temperature. This causes the onset of intrinsic carrier conduction to occur at higher temperatures, thereby suppressing bipolar conduction. The reason for the band gap increase may be related to the recent discovery that the Pb atoms are in fact displaced off the octahedron center in the rock salt structure, causing increases with rising temperature.[43] Because of the negligible bipolar diffusion, the *ZT* values may continue to rise with increasing temperature, and, for this reason, measurements on selected samples were extended to a temperature of 923 K. These measurements are challenging because of evaporation of sulfur occurring at >750 K. To suppress the evaporation, we developed a coating technique that overlays a thin boron nitride (BN) layer (thickness is 0.1−0.2 mm) on the samples. The BN coating allows for stable and repeatable measurements to be carried out for an extended period of time.

Figure 11 shows the thermoelectric properties for the optimized samples of $Pb_{0.975}Na_{0.025}S$ with 3.0% SrS/CaS up to 923 K. The electrical conductivities of all samples exhibit the same temperature-dependent trend, as shown in Figure 11a. The Seebeck coefficient temperature dependence is similar because all samples have similar Na doping concentrations. Remarkably, no sign of saturation in the Seebeck coefficient is evident up to 923 K, see Figure 11b, resulting in all power factors peaking at 923 K (Figure 11c). The total thermal conductivity of this sample series shows a significant decrease with increasing temperature for both the SrS and the CaS containing samples (Figure 11d). (Heat capacity, thermal diffusivity, Lorenz number, and electronic thermal conductivity for these samples can be found in the Supporting Information, Figure S9.) This falling trend is also reflected in the lattice thermal conductivity (Figure 11e). The lattice thermal conductivity at 923 K for the $Pb_{0.975}Na_{0.025}S$ samples with 3.0% SrS and 3.0% CaS reaches 0.60 and ∼0.57 W m^{-1} K^{-1}, respectively. These values are comparable to those of p-type $AgPb_mSn_nSbTe_{m+n+2}$[12] and p-type PbTe−SrTe.[15] It is interesting to note that these lattice thermal conductivity values are still much higher than the "minimal lattice thermal conductivity" value of ∼0.36 W m^{-1} K^{-1} for bulk PbTe as calculated by Koh et al.[44] This seems to leave additional room for further reductions. As shown in Figure 11f, a *ZT* value of 1.20 at 923 K is achieved for the $Pb_{0.975}Na_{0.025}S$ sample with 3.0% SrS and ∼1.12 for the $Pb_{0.975}Na_{0.025}S$ sample with 3.0% CaS. These *ZT* values are the highest ever reported for lead sulfide materials. They are slightly higher than those of n-type PbS with *x*% Bi_2S_3 reported recently[21] and similar to those reported for p-type PbSe.[19] Although our experimental setup did not allow us to measure above 923 K, we believe the trend will continue above 1000 K, reaching *ZT* of 1.3−1.4.

4. Thermal Stability of $Pb_{0.975}Na_{0.025}S$ with 3.0% SrS (CaS). To check the temporal stability of the high-performance samples at elevated temperature, we annealed the best performing samples ($Pb_{0.975}Na_{0.025}S$ samples with 3.0% SrS/CaS) at 723 K for 15 d. As shown in Figure 11f, the *ZT* values for the annealed samples not only did not deteriorate but improved, even though this small improvement falls within the uncertainty of the *ZT* calculation. After a 15 d annealing treatment, the *ZT* value at 923 K for the $Pb_{0.975}Na_{0.025}S$ sample with 3.0% SrS increased to ∼1.22, and that of the $Pb_{0.975}Na_{0.025}S$ sample with 3.0% CaS rose to ∼1.15. The

dx.doi.org/10.1021/ja301772w | *J. Am. Chem. Soc.* 2012, 134, 7902−7912

improvement of ZT after annealing is caused by the further reduction in thermal conductivity (Figure 11d) and the nearly unchanged power factor (Figure 11c). The reduction of the thermal conductivity is attributed to the small decrease in electrical conductivity (Figure 11a) and a corresponding small increase in the Seebeck coefficient (Figure 11b). The latter may be due to a slight loss of sulfur from the PbS samples during annealing. Nevertheless, the annealed samples showed no visible changes such as bubbles, bloating,[45] cracks, or color changes on the surface and appeared to be of the same quality as before annealing, Figure S1 (see the Supporting Information for photographs of annealed samples). This behavior is similar to the enhanced properties observed for annealed $Ag_{0.8}Pb_{22.5}SbTe_{20}$,[8] in which the inherent nanostructuring is improved by annealing that further reduces the lattice thermal conductivity. Besides annealing treatments, the thermal stability is also suggested from the fact that the heating and cooling cycles gave repeatable thermoelectric properties up to 923 K, as shown in Figure 11.

CONCLUDING REMARKS

We demonstrated for the first time that p-type PbS, an inexpensive, Te-free material, can achieve a high ZT value of 1.2 at 923 K. The ZT trend is expected to continue past 1000 K and reach 1.3 or higher. The high performance of PbS was accomplished by shifting the power factor maximum to a higher temperature via tuning the carrier concentration and greatly reducing the lattice thermal conductivity by introduction of nanostructured second phases. We have identified a highly effective type of nanostructuring using SrS and CaS as second phases coupled with powder SPS processing. The high performance is characterized by excellent thermal stability as suggested by the annealing treatment. The promising thermoelectric properties indicate that PbS is a robust alternative for PbTe and PbSe thermoelectric materials for high temperature power generation applications.

In p-type PbS, both nanoscale precipitates and point defects play an important role in reducing the lattice thermal conductivity. The contribution from nanoscale precipitates of SrS is greater than those of CaS, whereas the contribution of point defects in the case of CaS is larger than for SrS. The lowest lattice thermal conductivity for the best performing samples observed in this work is ~0.57 W m^{-1} K^{-1} at 923 K, which is the lowest value ever reported for PbS. This is still higher, however, than the "minimal lattice thermal conductivity" value of ~0.36 W m^{-1} K^{-1} for bulk PbTe calculated by Koh et al.[44] Therefore, even better thermoelectric performance from PbS can be expected by (a) using more effective methods for reducing the lattice thermal conductivity to reach 0.36 W m^{-1} K^{-1}, and (b) increasing the Seebeck coefficient and the power factor through the incorporation of elements creating electronic band structure modifications.[46] With both n- and p-type PbS-based thermoelectrics now reaching ZT_{max} of at least ~1.1 and 1.22, respectively, at ~925 K, the path is opened for contemplating thermoelectric generators made of these truly inexpensive materials. On the basis of the thermoelectric conversion efficiency, eq 5:

$$\eta = \frac{\Delta T}{T_{hot}} \frac{\sqrt{1 + ZT_{avg}} - 1}{\sqrt{1 + ZT_{avg}} + \frac{T_{cold}}{T_{hot}}} \quad (5)$$

where T_{hot} and T_{cold} are the temperatures of the hot and cold ends in a thermoelectric module, respectively, and ΔT their difference, an ideal such device operating at 923 K with T_{cold} of 400 K could produce electricity at nearly 11% efficiency. This is very significant given that the materials are based on widely abundant earth elements. Finally, one may suggest that the presence of lead in PbS makes the material toxic. This is not the case.[47] Being made of nontoxic elements does not necessarily make a compound nontoxic (e.g., Zn_3P_2 is made of nontoxic elements but itself is highly toxic, e.g., rat poison). Conversely, being made of toxic elements does not necessarily make a compound toxic. Rather it is the actual chemical form and bioavailability that makes it so. The lead in PbS is extremely strongly bound, not bioavailable, and therefore we submit PbS is likely nontoxic.

ASSOCIATED CONTENT

Supporting Information

Lorenz number calculation details. Photograph for the typical samples in this study annealed at 723 K for 15 days (Figure S1); photographs for typical samples coated by a thin boron nitride (BN) layer in stages (Figure S2); thermoelectric properties as a function of temperature for PbS with x% Na doping including heat capacity, thermal diffusivity, Lorenz number, and electronic thermal conductivity (Figure S3); powder XRD patterns of $Pb_{0.975}Na_{0.025}S$ with x% SrS (Figure S4); thermoelectric properties as a function of temperature for $Pb_{0.975}Na_{0.025}S$ with x% SrS including heat capacity, thermal diffusivity, Lorenz number, and electronic thermal conductivity (Figure S5); powder XRD patterns of $Pb_{0.975}Na_{0.025}S$ with x% CaS (Figure S6); thermoelectric properties as a function of temperature for $Pb_{0.975}Na_{0.025}S$ with x% CaS including heat capacity, thermal diffusivity, Lorenz number, and electronic thermal conductivity (Figure S7); Hall coefficient, R_H, as a function of temperature for heavy hole doped p-type PbS samples with varied carrier concentrations (Figure S8); and thermoelectric properties up to 923 K as a function of temperature for $Pb_{0.975}Na_{0.025}S$ with 3.0% SrS/CaS with and without annealing treatment including heat capacity, thermal diffusivity, Lorenz number, and electronic thermal conductivity (Figure S9). This material is available free of charge via the Internet at http://pubs.acs.org.

AUTHOR INFORMATION

Corresponding Author

m-kanatzidis@northwestern.edu

Author Contributions

#These authors contributed equally.

Notes

The authors declare no competing financial interest.

ACKNOWLEDGMENTS

This work was supported by grant DOE-EERE/NSF grant CBET-1048728 (L.-D.Z. and M.G.K.). The transmission electron microscopy, SPS, and Hall measurements in this work were supported as part of the Revolutionary Materials for Solid State Energy Conversion, an Energy Frontier Research Center funded by the U.S. Department of Energy, Office of Science, and Office of Basic Energy Sciences under Award Number DE-SC0001054 (T.P.H., V.P.D., J.H., X.Z., and C.U.). Transmission electron microscopy work was performed in the (EPIC) (NIFTI) (Keck-II) facility of NUANCE Center at

Northwestern University. The NUANCE Center is supported by NSF-NSEC, NSF-MRSEC, Keck Foundation, the State of Illinois, and Northwestern University. We acknowledge use of the Office of Naval Research DURIP-supported Pulsed Electric Current Sintering System at Michigan State University.

REFERENCES

(1) (a) Kanatzidis, M. G. *Chem. Mater.* **2010**, *22*, 648. (b) Sootsman, J. R.; Chung, D.-Y.; Kanatzidis, M. G. *Angew. Chem., Int. Ed.* **2009**, *48*, 8616. (c) Kanatzidis, M. G. *Semicond. Semimetals* **2000**, *69*, 51. (d) Vineis, C. J.; Shakouri, A.; Majumdar, A.; Kanatzidis, M. G. *Adv. Mater.* **2010**, *22*, 3970. (e) Kanatzidis, M. G. *Recent Trends In Thermoelectric Materials Research I Book Series: Semiconductors And Semimetals*; Academic Press: San Diego CA, 2000, *69*, 51.

(2) (a) Li, J.-F.; Liu, W. S.; Zhao, L.-D.; Zhou, M. *NPG Asia Mater.* **2010**, *2*, 152. (b) Snyder, J. G.; Toberer, E. S. *Nat. Mater.* **2008**, *7*, 105. (c) Chen, G.; Dresselhaus, M. S.; Dresselhaus, G.; Fleurial, J.-P.; Caillat, T. *Int. Mater. Rev.* **2003**, *48*, 45. (d) Dresselhuas, M. S.; Chen, G.; Tang, M.; Yang, R.; Lee, H.; Wang, D.; Ren, Z.; Fleurial, J.; Gogna, P. *Adv. Mater.* **2007**, *19*, 1043. (e) Sootsman, J. R.; Kong, H.; Uher, C.; D'Angelo, J.; Wu, C. I.; Hogan, T. P.; Caillat, T.; Kanatzidis, M. G. *Angew. Chem., Int. Ed.* **2008**, *47*, 8618.

(3) Liu, W.-S.; Zhang, Q.; Lan, Y.; Chen, S.; Yan, X.; Zhang, Q.; Wang, H.; Wang, D.; Chen, G.; Ren, Z. F. *Adv. Energy Mater.* **2011**, *1*, 577.

(4) Poudel, B.; Hao, Q.; Ma, Y.; Lan, Y.; Minnich, A.; Yu, B.; Yan, X.; Wang, D.; Muto, A.; Vashaee, D.; Chen, X.; Liu, J.; Dresselhaus, M. S.; Chen, G.; Ren, Z. F. *Science* **2008**, *320*, 634.

(5) Wang, X. W.; Lee, H.; Lan, Y. C.; Zhu, G. H.; Joshi, G.; Wang, D. Z.; Yang, J.; Muto, A. J.; Tang, M. Y.; Klatsky, J.; Song, S.; Dresselhaus, M. S.; Chen, G.; Ren, Z. F. *Appl. Phys. Lett.* **2008**, *93*, 193121.

(6) Joshi, G.; Lee, H.; Lan, Y.; Wang, X.; Zhu, G.; Wang, D.; Gould, R. W.; Cuff, D. C.; Tang, M. Y.; Dresselhaus, M. S.; Chen, G.; Ren, Z. F. *Nano Lett.* **2008**, *8*, 4670.

(7) Hsu, K. F.; Loo, S.; Guo, F.; Chen, W.; Dyck, J. S.; Uher, C.; Hogan, T.; Polychroniadis, E. K.; Kanatzidis, M. G. *Science* **2004**, *303*, 818.

(8) Zhou, M.; Li, J.-F.; Kita, T. *J. Am. Chem. Soc.* **2008**, *130*, 4527.

(9) Androulakis, J.; Lin, C.-H.; Kong, H.-J.; Uher, C.; Wu, C.-I.; Hogan, T.; Cook, B. A.; Caillat, T.; Paraskevopoulos, K. M.; Kanatzidis, M. G. *J. Am. Chem. Soc.* **2007**, *129*, 9780.

(10) Ahn, K.; Han, M. K.; He, J. Q.; Androulakis, J.; Ballikaya, S.; Uher, C.; Dravid, V. P.; Kanatzidis, M. G. *J. Am. Chem. Soc.* **2010**, *132*, 5227.

(11) Pei, Y. Z.; Lensch-Falk, J.; Toberer, E. S.; Medlin, D. L.; Snyder, G. J. *Adv. Funct. Mater.* **2010**, *20*, 764.

(12) (a) Androulakis, J.; Hsu, K.-F.; Pcionek, R.; Kong, H.; Uher, C.; D'Angelo, J. J.; Downey, A.; Hogan, T.; Kanatzidis., M. G. *Adv. Mater.* **2006**, *18*, 1170. (b) Bilc, D.; Mahanti, S. D.; Quarez, E.; Hsu, K. F.; Pcionek, R.; Kanatzidis, M. G. *Phys. Rev. Lett.* **2004**, 93146403.

(13) Pei, Y. Z.; Shi, X. Y.; LaLonde, A.; Wang, H.; Chen, L. D.; Snyder, G. J. *Nature* **2011**, *473*, 66.

(14) Poudeu, P. F. P.; D'Angelo, J. J.; Downey, A. D.; Short, J. L.; Hogan, T. P.; Kanatzidis, M. G. *Angew. Chem., Int. Ed.* **2006**, *45*, 3835.

(15) Biswas, K.; He, J. Q.; Zhang, Q. C.; Wang, G. Y.; Uher, C.; Dravid, V. P.; Kanatzidis, M. G. *Nat. Chem.* **2011**, *3*, 160.

(16) Girard, S. N.; He, J. Q.; Zhou, X. Y.; Shoemaker, D.; Jaworski, C. M.; Uher, C.; Dravid, V. P.; Heremans, J. P.; Kanatzidis, M. G. *J. Am. Chem. Soc.* **2011**, *133*, 16588.

(17) Androulakis, J.; Todorov, I.; He, J. Q.; Chung, D.-Y.; Dravid, V. P.; Kanatzids, M. G. *J. Am. Chem. Soc.* **2011**, *133*, 10920.

(18) Androulakis, J.; Yeseul, L.; Todorov, I.; Chung, D.-Y.; Kanatzids, M. G. *Phys. Rev. B* **2011**, *83*, 195209.

(19) Wang, H.; Pei, Y. Z.; Lalonde, A. D.; Snyder, G. J. *Adv. Mater.* **2011**, *23*, 1366.

(20) Johnsen, S.; He, J. Q.; Androulakis, J.; Dravid, V. P.; Todorov, I.; Chung, D.-Y.; Kanatzidis, M. G. *J. Am. Chem. Soc.* **2011**, *133*, 3460.

(21) Zhao, L.-D.; Lo, S.-H.; He, J. Q.; Li, H.; Biswas, K.; Androulakis, J.; Wu, C.-I.; Hogan, T. P.; Chung, D.-Y.; Dravid, V. P.; Kanatzidis, M. G. *J. Am. Chem. Soc.* **2011**, *133*, 20476.

(22) (a) Zhao, L.-D.; Zhang, B. P.; Li, J.-F.; Zhou, M.; Liu, W.-S.; Liu, J. *J. Alloys Compd.* **2008**, *455*, 259. (b) Zhao, L.-D.; Zhang, B. P.; Liu, W.-S.; Zhang, H. L.; Li, J.-F. *J. Solid State Chem.* **2008**, *181*, 3278. (c) Zhao, L.-D.; Zhang, B. P.; Li, J.-F.; Zhang, H. L.; Liu, W. S. *Solid State Sci.* **2008**, *10*, 651.

(23) (a) Zhang, Q.; He, J.; Zhu, T. J.; Zhang, S. N.; Zhao, X. B.; Tritt, T. M. *Appl. Phys. Lett.* **2008**, *93*, 102109. (b) Zhang, Q.; He, J.; Zhao, X. B.; Zhang, S. N.; Zhu, T. J.; Yin, H.; Tritt, T. M. *J. Phys. D* **2008**, *41*, 185103.

(24) (a) Liu, W. S.; Zhang, B. P.; Zhao, L.-D.; Zhang, H. L.; Li, J.-F. *Chem. Mater.* **2008**, *20*, 7526. (b) Zhao, W. Y.; Wei, P.; Zhang, Q. J.; Dong, C. L.; Liu, L. S.; Tang, X. F. *J. Am. Chem. Soc.* **2009**, *131*, 3713. (c) Li, H.; Tang, X. F.; Zhang, Q.; Uher, C. *Appl. Phys. Lett.* **2009**, *94*, 102114.

(25) Cox, P. A. *The Elements: Their Origin, Abundance, and Distribution*; Oxford University Press: Oxford, 1989.

(26) Blachnik, R.; Igel, R. *Z. Naturforsch., B* **1974**, *29*, 625.

(27) Fitsul, V. I. *Heavily Doped Semiconductors*; Plenum Press: New York, 1969.

(28) Kumar, G. S.; Prasad, G.; Pohl, R. O. *J. Mater. Sci.* **1993**, *8*, 4261.

(29) Callayway, J.; Von Baeyer, H. C. *Phys. Rev.* **1960**, *120*, 1149.

(30) Dey, T. K.; Chaudhuri, K. D. *J. Low Temp. Phys.* **1976**, *23*, 419.

(31) Yang, J.; Meisner, G. P.; Chen, L. *Appl. Phys. Lett.* **2004**, *85*, 1140.

(32) Wan, C. L.; Pan, W.; Xu, Q.; Qin, Y. X.; Wang, J. D.; Qu, Z. X.; Fang, M. H. *Phys. Rev. B* **2006**, *74*, 144109.

(33) Ravich, I. I.; Efimova, B. A.; Smirnov, I. A. *Semiconducting Lead Chalcogenides*; Plenum Press: New York, 1970.

(34) Zhao, L.-D.; Zhang, B. P.; Liu, W.-S.; Li, J.-F. *J. Appl. Phys.* **2009**, *105*, 023704.

(35) Hoang, K.; Mahanti, S. D.; Kanatzidis, M. G. *Phys. Rev. B* **2010**, *81*, 115106.

(36) (a) Airapetyants, S. V.; Vinograd, M. N.; Dubrovsk, I. N.; Kolomoet, N. V.; Rudnik, I. M. *Sov. Phys. Solid State USSR* **1966**, *8*, 1069. (b) Chernik, I. A.; Kaidanov, V. I.; Vinogradova, M. I.; Kolomoets, N. V. *Sov. Phys.-Semiconductors* **1968**, *2*, 645. (c) Androulakis, J.; Todorov, I.; Chung, D.-Y.; Ballikaya, S.; Wang, G. Y.; Uher, C.; Kanatzids, M. G. *Phys. Rev. B* **2010**, *82*, 115209.

(37) (a) Singh, D. J. *Phys. Rev. B* **2010**, *81*, 195217. (b) Ahmad, S.; Mahanti, S. D.; Hoang, K.; Kanatzidis, M. G. *Phys. Rev. B* **2006**, *74*, 155205.

(38) Hytch, M. J.; Snoeck, E.; Kilaas, R. *Ultramicroscopy* **1998**, *74*, 131.

(39) He, J. Q.; Vasco, E.; Jia, C. L.; Wang, R. H. *Appl. Phys. Lett.* **2005**, *87*, 062901.

(40) He, J. Q.; Girard, S. N.; Kanatzidis, M. G.; Dravid, V. P. *Adv. Funct. Mater.* **2010**, *20*, 764.

(41) Smirnov, I. A.; Moizhes, B. Y.; Nensberg, E. D. *Sov. Phys.-Solid State* **1961**, *2*, 1793.

(42) Goldsmid, H. J. *Introduction to Thermoelectricity*; Springer Series in Materials Science; Springer: Heidelberg, 2010.

(43) Bozin, E.; Malliakas, C. D.; Souvatzis, P.; Proffen, T.; Spaldin, N. A.; Kanatzidis, M. G.; Billinge, S. J. L. *Science* **2010**, *330*, 1660.

(44) Koh, Y. K.; Vineis, C. J.; Calawa, S. D.; Walsh, M. P.; Cahill, D. G. *Appl. Phys. Lett.* **2009**, *94*, 153101.

(45) Ren, F.; Case, E. D.; Ni, J. E.; Timm, E. J.; Lara-Curzio, E.; Trejo, R. M.; Lin, C.-H.; Kanatzidis, M. G. *Philos. Mag.* **2009**, *89*, 143–167.

(46) Heremans, J. P.; Jovovic, V.; Toberer, E. S.; Saramat, A.; Kurosaki, K.; Charoenphakdee, A.; Yamanaka, S.; Snyder, G. J. *Science* **2008**, *321*, 554.

(47) Dieter, M. P.; Matthews, H. B.; Jeffcoat, R. A.; Moseman, R. F. *J. Toxicol. Environ. Health* **1993**, *39*, 79.